A 3-D Nanoelectrokinetic Model for Predictive Assembly of Nanowire Arrays using Floating Electrode Dielectrophoresis

Sachin K. Singh, [1] Nehal Aryaan, [1] Md Ruhul Amin Shikder, [1] Bryan W. Byles,[2] Ekaterina Pomerantseva,[2] and Arunkumar Subramanian*[1]

[1] Department of Mechanical and Industrial Engineering, University of Illinois at Chicago, Chicago, USA

[2] Department of Materials Science and Engineering, Drexel University, Philadelphia, Pennsylvania, 19104, USA.

*E-mail: sarun@uic.edu

Abstract

Floating electrode dielectrophoresis (FE-DEP) presents a promising avenue for scalable assembly of nanowire (NW) arrays on silicon chips and offers better control in limiting the number of deposited nanowires when compared with the conventional, two-electrode DEP process. This article presents a 3-D nanoelectrokinetic model, which calculates the imposed electric field and its resultant NW force / velocity maps within the region of influence of an electrode array operating in the FE-DEP configuration. This enables the calculation of NW trajectories and their eventual localization sites on the target electrodes as a function of parameters such as NW starting position, NW size, the applied electric field, suspension concentration, and deposition time. The accuracy of this model has been established through a direct quantitative comparison with the assembly of manganese dioxide nanowire arrays. Further analysis of the computed data reveals interesting insights into the following aspects: (a) asymmetry in NW localization at electrode sites, and (b) the workspace regions from which NWs are drawn to assemble such that their center-of-mass is located either in the inter-electrode gap region (desired) or on top of one of the assembly electrodes (undesired). This analysis is leveraged to outline a strategy, which involves a physical confinement of the NW suspension within lithographically patterned reservoirs during assembly, for single NW deposition across large arrays with high estimated assembly yields on the order of 87%.

1. Introduction

The synthesis process for one-dimensional (1-D) nanomaterials such as nanowires and nanotubes typically yields a powder where these materials are strongly agglomerated together under the dominating influence of van-der-Waals' interactions. The isolation of individual nanomaterials from these agglomerated powders and their integration into functional device arrays on substrates such as silicon chips is an important technological need for diverse application areas, which include energy [1-4], nanoelectronics [5-7], and sensing [8-11]. In recent years, directed-field, bottom-up assembly techniques have emerged as one of the

key approaches for such device integration at the single nanowire or nanotube level. These techniques have employed different types of external stimuli such as electric [3-6, 8-19], magnetic [20, 21], optical [22-24] and acoustic fields [25], among others, to accomplish the nanoassembly process.

Among these directed-field nanoassembly techniques, dielectrophoresis [3-6, 8-19, 26], which involves the use of an electric field gradient to polarize and drive nanomaterials towards suitably engineered regions of field maxima on target substrates, offers a numbers of advantages: (a) it works with any material system as long as it is sufficiently more polarizable than the suspension medium and hence, is used to manipulate a wide variety of nanomaterials ranging from metals to semiconductors and ceramics, (b) it is simple to implement on silicon chips due to an ability to precisely engineer the assembly fields using micro- / nanomachined electrodes, (c) it does not require complex pieces of equipment, control electronics, or environmental chambers, (d) it yields assembly of the nanomaterial on top of conductive pads or electrodes, which is a desired configuration for material probing in most technological applications, and (e) it yields material deposition at room-temperature and in a scalable fashion over short deposition time frames on the order of a few seconds to minutes. At the same time, barriers remain for DEP-based nanoassembly techniques in terms of achieving suitable control over process metrics in order to yield single NW assembly. This article presents an electrokinetic model that advances physical confinement of the precursor suspension within suitable regions of the assembly workspace as a potential solution to this key problem.

A typical dielectrophoresis process is illustrated in Figure 1. In this method, a homogenous colloidal suspension of nanowires, which is prepared through ultrasonication in a solvent such as ethanol, is placed on a silicon chip with pre-patterned electrodes. When an electric field is applied across the electrodes through the generation of an electrical bias, the NWs in the suspension are polarized and attracted towards the electric field maxima, which are located near the electrode surfaces. After the nanowires are localized on the electrodes, the suspension is removed by nitrogen blow-drying and the trapped nanowires are held in place through van-der Waals interactions with the electrode surface.

In terms of the electrode biasing design, dielectrophoresis can be classified into two categories: conventional DEP (C-DEP) and floating electrode dielectrophoresis (FE-DEP) (Figure 1). C-DEP [3, 5, 6, 8-13, 17, 19] employs a two-electrode design where the assembly field is generated by applying an electrical bias directly between an array of opposing pairs of electrodes. On the other hand, FE-DEP [4, 14-16, 18, 26] involves the use of an array of assembly electrode pairs, where only one set of electrodes is tied to the assembly bias (Figure 1(b)). The opposing set of FE-DEP electrodes is held at a floating potential with respect to an underlying substrate, which is electrically grounded and serves as the third electrode during nanoassembly. Thus, the electrical circuit during FE-DEP involves an additional capacitive impedance between the floating and ground electrodes, which grows in importance as nanowires are captured at an assembly site and thereby, substantially slows down the capture of nanowires beyond the first deposition, unless the suspension concentration and / or assembly bias are high enough to yield near-simultaneous assembly of multiple nanowires. This FE-DEP approach has been employed over the past decade to demonstrate a relatively better control over single nanomaterial assembly across electrodes (as compared to C-DEP).

While there have been multiple experimental reports on the use of FE-DEP, including from the authors of this current effort [4, 14, 26-27], there has been no past effort on quantitative modeling of FE-DEP in three dimensions. Such a model is essential to move towards a predictive nanoassembly regime that accounts for all of the process parameters such as electrode design, applied electric field, NW size, NW starting position in the workspace, suspension concentration, and deposition time. This report addresses this need and makes the following contributions: (i) it employs a 3-D nanoelectrokinetic model to determine NW trajectories and localization sites on electrodes as a function of all relevant FE-DEP assembly parameters, (ii) this effort considers the impact of the entire electrode array design on the resultant assembly process through the choice of appropriate boundary conditions on simulation workspace. This is in contrast to past reports where the computational models have predominantly considered single electrode locations in isolation while
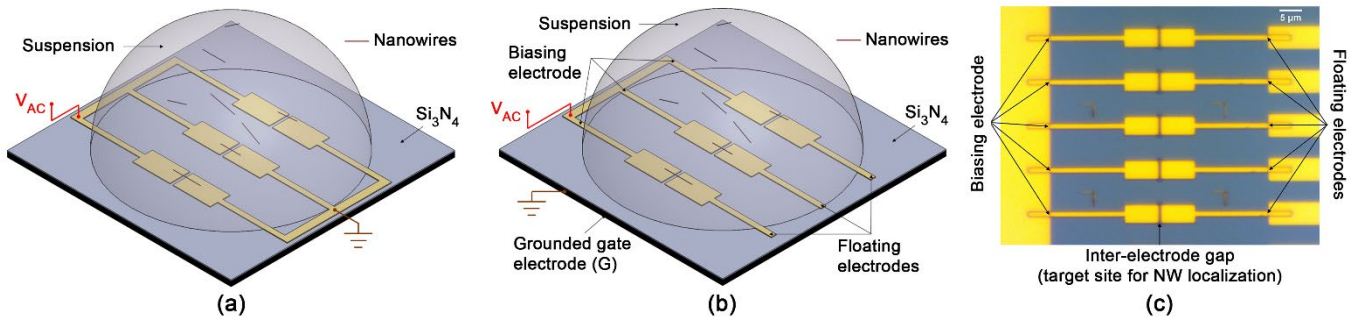

Figure 1: Schematic illustration of the DEP process and its electrode biasing design classification. (a) C-DEP chip design, (b) FE-DEP chip design, and (c) Optical micrograph of a fabricated FE-DEP chip with an array of electrode pairs on to which NWs are deposited. Scale bar = 5μm.

neglecting the impact of neighboring electrodes [27, 28], (iii) this report establishes a quantitative correlation between models and experimental data, and thereby, establishes a pathway for quantitative prediction of assembly performance metrics, and (iv) it reveals interesting insights into the asymmetry in NW localization at electrode sites and into the suspension volume from which NWs are drawn to assemble such that their center-of-mass is located either in the inter-electrode gap regions (desired) or on top of one of the assembly electrodes (undesired). This analysis is leveraged to outline a strategy, which involves a physical confinement of the NW suspension within lithographically patterned reservoirs during assembly, for single NW deposition across large arrays with estimated assembly yields on the order of 87%. The results presented in this article are expected to provide predictive guidelines for design / fabrication of NW assembly platforms and thereby, advance this capability further towards integration with conventional IC nanomachining process flows.

2. 3-D Nanoelectrokinetic Model

A 3-D computational model has been built for understanding the FE-DEP assembly of NWs over an on-chip platform. This model has also been complemented by DEP experiments for NW assembly on a similar on-chip platform.

The on-chip platform (Figure 1(b-c)) consists of a silicon substrate, which is coated with a 100nm layer of silicon nitride (Si_3N_4). An array of opposing pairs of gold nano-electrodes is patterned over this nitride film. The nitride layer acts as an insulation barrier between the silicon substrate and the patterned gold nano-electrode array. The electrodes on the left-side of the array serve as the biasing electrodes and are held at a common AC bias. The opposing electrodes (i.e., on the right-side) are maintained at a floating potential. The underlying silicon substrate is connected to the electrical ground.

To computationally model the FE-DEP assembly of NWs under the action of dielectrophoretic forces, the electric field distribution, which is generated within the chip design of Figure 1(b-c), is first calculated using a fine element model in COMSOL® Multiphysics 5.3 software. The simulation workspace is chosen as a rectangular volume unit cell that extends up to a height of 50μm from the electrode surface (Figure 2(a)). This unit cell contains a single electrode pair at its center and extends up to the mid-point of the region that separates the electrode pair from its nearest neighbours on either side. The influence of the experimental array design is replicated in the simulated single-electrode unit-cell by imposing a symmetry (or, zero charge) boundary condition on the planes, which pass through the middle of this separation
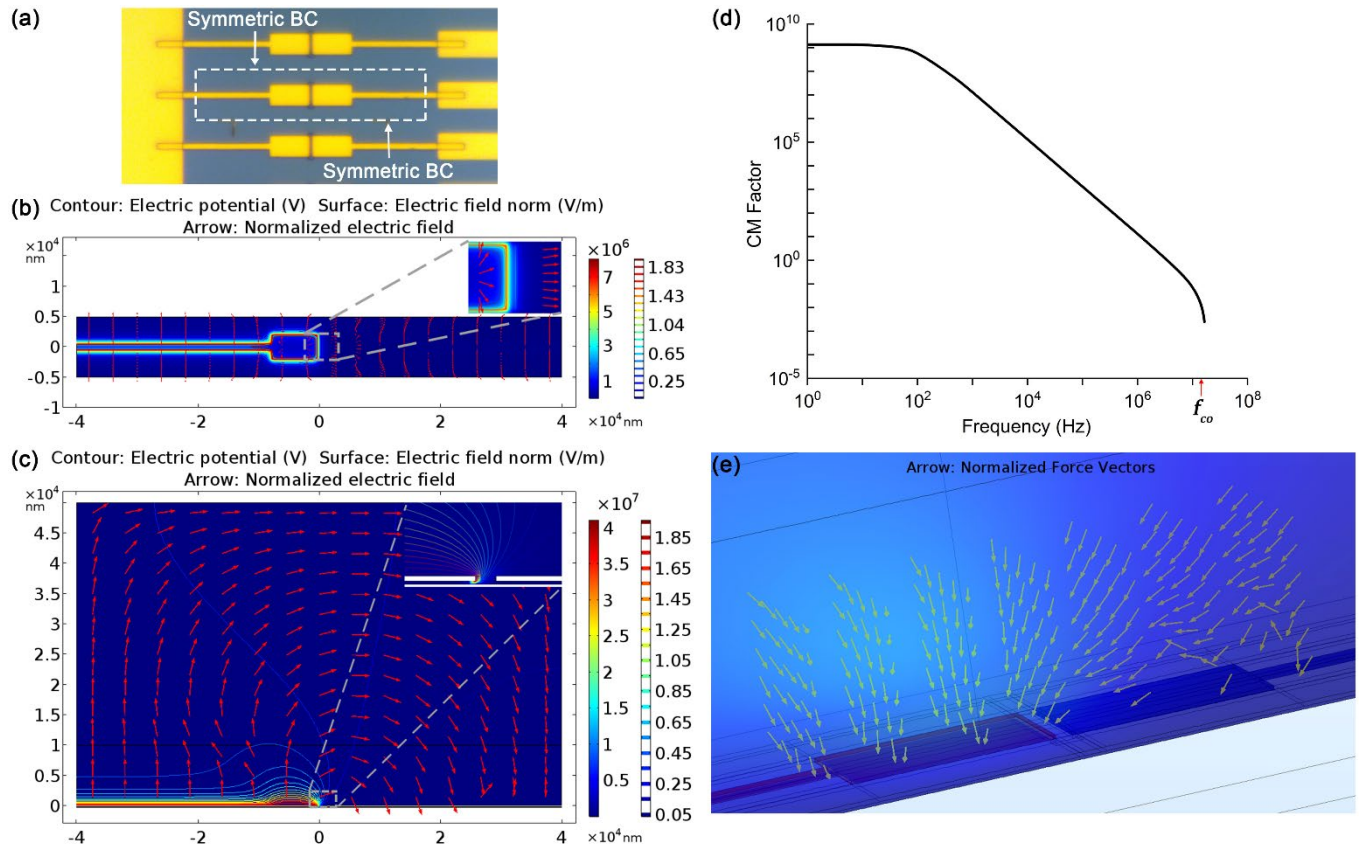

Figure 2: (a) A 3-D unit cell, which contains a single electrode pair and extends up to the mid-point of its separation region with respect to the neighbouring electrode pairs, is utilized as the simulation workspace, (b) Top-view of the computed electric-field distribution within the simulation workspace, (c) Side-view of the electric-field distribution at a plane, which passes through the electrode center-line. The inset images in panels 'b' and 'c' show a zoomed-in view of the inter-electrode gap region. These insets show that the field maxima is asymmetrically located in the inter-electrode gap region and remains near the edges of the biasing electrode, (d) Claussius-Massotti factor as a function of frequency, and (e) the normalized force vectors showing the direction of NW motion during FE-DEP assisted assembly.

region between the neighbouring electrode pairs. Thus, through an appropriate choice for the simulation workspace and its boundary conditions, the model isolates the region of exclusive influence of a single electrode pair while accounting for the influence of the other electrode pairs in the array (which occurs at the workspace boundaries).

Furthermore, this study employed a suspension of α-MnO$_2$ NWs in ethanol as the model system for both, simulations and experiments. The choice of this material system was motivated by their relevance as candidates for use in next-generation battery cathodes [29], supercapacitors [30], and molecular sieves [31]. These α-MnO$_2$ NWs were synthesized using a hydrothermal process outlined in Ref. [32] and yielded NWs without any systematic dimensional tapering effects or embedded catalysts. The DEP localization of these nanomaterials within the on-chip platform will enable the characterization of their electrical and mechanical properties at the single particle level. Furthermore, the models assume a nominal NW diameter of 20nm, since this represents the mid-range of diameters observed within the experimentally synthesized / assembled samples.

The electric field distribution within the simulation workspace was calculated using a COMSOL-based finite-element model and is shown in Figure 2(b-c) for an applied voltage of 2V. From these images, it is evident that the largest field gradients appear near the biasing electrode edges (i.e., on the left-hand side). Thus, the electric field distribution is asymmetric with respect to the two electrodes due to the FE-DEP biasing design and this is another key difference from past reports involving C-DEP analysis [33, 34]. This field distribution is subsequently used in a MATLAB 2017b script to calculate the DEP forces acting within the chosen workspace region. For calculation of forces, the NW is approximated as a prolate ellipsoid with its length much larger than its diameter. The time averaged DEP force acting on a NW is given by [35, 36]:

$$F_{DEP} = \frac{3}{2}\pi r^2 l\varepsilon_m Re\{K\}\nabla(E.E^*) \qquad (1)$$

where, r, l, E and E^* represent the NW radius, NW length, the computed electric field and its complex conjugate, respectively. In addition, K denotes the Claussius Massotti (CM) factor, which is a measure of the relative polarizability of the NW with respect to the medium (i.e., ethanol), and is defined as [19, 37]:

$$K = \frac{\tilde{\varepsilon}_{NW} - \tilde{\varepsilon}_m}{\tilde{\varepsilon}_m} \qquad (2)$$

where, $\tilde{\varepsilon}_{NW}$ and $\tilde{\varepsilon}_m$ are the complex permittivity of the NW and the suspension medium, respectively. The complex permittivity of the NW and medium are calculated using their real dielectric permittivity (ε), conductivity (σ) and applied field frequency (ω), as given below:

$$\tilde{\varepsilon} = \varepsilon - i\frac{\sigma}{\omega} \qquad (3)$$

Assuming the electric field to be constant along the length of the NW and spatially invariant in phase, equation (1) can be rewritten as:

$$F_{DEP} = \frac{3}{2}\pi r^2 l\varepsilon_m Re\{K\}\nabla|E|^2 \qquad (4)$$

It can be seen from equation (4) that the DEP force acting on the suspended NW is directly proportional to the real part of the CM factor. The CM factor has been plotted as a function of excitation frequency in Figure 2(d). These calculations have assumed the values of 2.07×10^{-10} F/m, 2.17×10^{-10} F/m, 182.2 S/m, and 1.35×10^{-7} S/m for ε_{NW}, ε_m, σ_{NW} ,and σ_m, respectively. When the CM factor is positive, the α-MnO$_2$ NWs are more polarizable than ethanol and are pushed towards the electric field maxima due to positive dielectrophoresis. This occurs below the crossover frequency (f_{CO}); and at higher frequencies, the NWs are pushed away from the electrode surfaces due to negative dielectrophoresis. In a previous report on 2-D models involving α-MnO$_2$ NWs in ethanol, we had established that operating in the near but, sub-threshold regime of this crossover frequency provides the best avenue for controllably manipulating individual nanowires towards successful trapping on the electrodes [27]. In order to stay within this sub-threshold frequency regime, we have chosen a 1MHz excitation frequency for all models / experiments employed in this report, and further details on the rationale underlying this regime can be found in Ref. [27].

The DEP force field within the simulation workspace, which encompasses a single unit-cell, is computed using a MATLAB code (based on equation (4)) and the normalized force vectors are shown in Figure 2(e). It can be seen that for most locations around the electrode pair, the DEP force acts on NWs in such a way that they are attracted either towards the biasing electrode surface (i.e., the electrode on the left-hand side) or towards the electrode gap. The contribution from inertial effects have been neglected in this computational model, as the characteristic time constant for motion due to inertial effects is much smaller than that due to DEP forces [38].

The dielectrophoretic motion of NWs through the suspension is resisted by a frictional drag force, which arises from the viscosity of the fluid. This drag force is accounted within the model by calculating the average friction factor f experienced by the prolate ellipsoid [39, 40], which is given as:

$$f = \frac{3\pi\eta l}{\ln(l/r)} \qquad (5)$$

where η is the viscosity of suspension medium. The velocity of the NW (v) at any point in the workspace is then computed as:

$$v = \frac{F_{DEP}}{f} \qquad (6)$$

In addition, the non-uniform electric field generates an electro-orientation torque that tends to align the NWs along the direction of the electric field. This time averaged torque acting can be obtained as:

$$T_z = \frac{1}{2}\pi r^2 l \varepsilon_m E^2 \sin\theta \cos\theta \operatorname{Re}\left(\frac{(\check{\varepsilon}_p - \check{\varepsilon}_m)^2}{\check{\varepsilon}_m(\check{\varepsilon}_m + \check{\varepsilon}_p)}\right) \qquad (7)$$

The resultant rotation of the NW is dependent on the interaction of electrorotational torque and the drag torque due to viscous drag on the NW. The angular velocity of the NW is defined is given as:

$$\omega_z = \frac{T_z}{f_\theta} \qquad (8)$$

where, the rotational frictional factor (f_θ) of the NW is defined as [40]:

$$f_\theta = \frac{2}{3}\pi\eta \frac{(l^2 + 4r^2)l}{2\ln(l/r) - 1} \qquad (9)$$

Thus, equation (6 and 8) enables the calculation of translational and angular velocity fields, which exist within the FE-DEP simulation workspace for a NW with a given dimension / size. From this translational and angular velocity field distribution for a NW, we can calculate its trajectory, its eventual trapping location on the electrode surface, its orientation, and its deposition time. The trajectories, which are estimated by this approach, for a NW that is 20nm in diameter and 2µm in length are plotted for six different starting positions of the NW within the FE-DEP workspace (Figure 3(a)). It can be seen that for four of these starting positions, the NW is in contact only with the biasing (or, left-side) electrode, due to the asymmetry in the FE-DEP electric-field gradients and hence, results in an undesired assembly outcome. For the remaining two starting positions, the NW
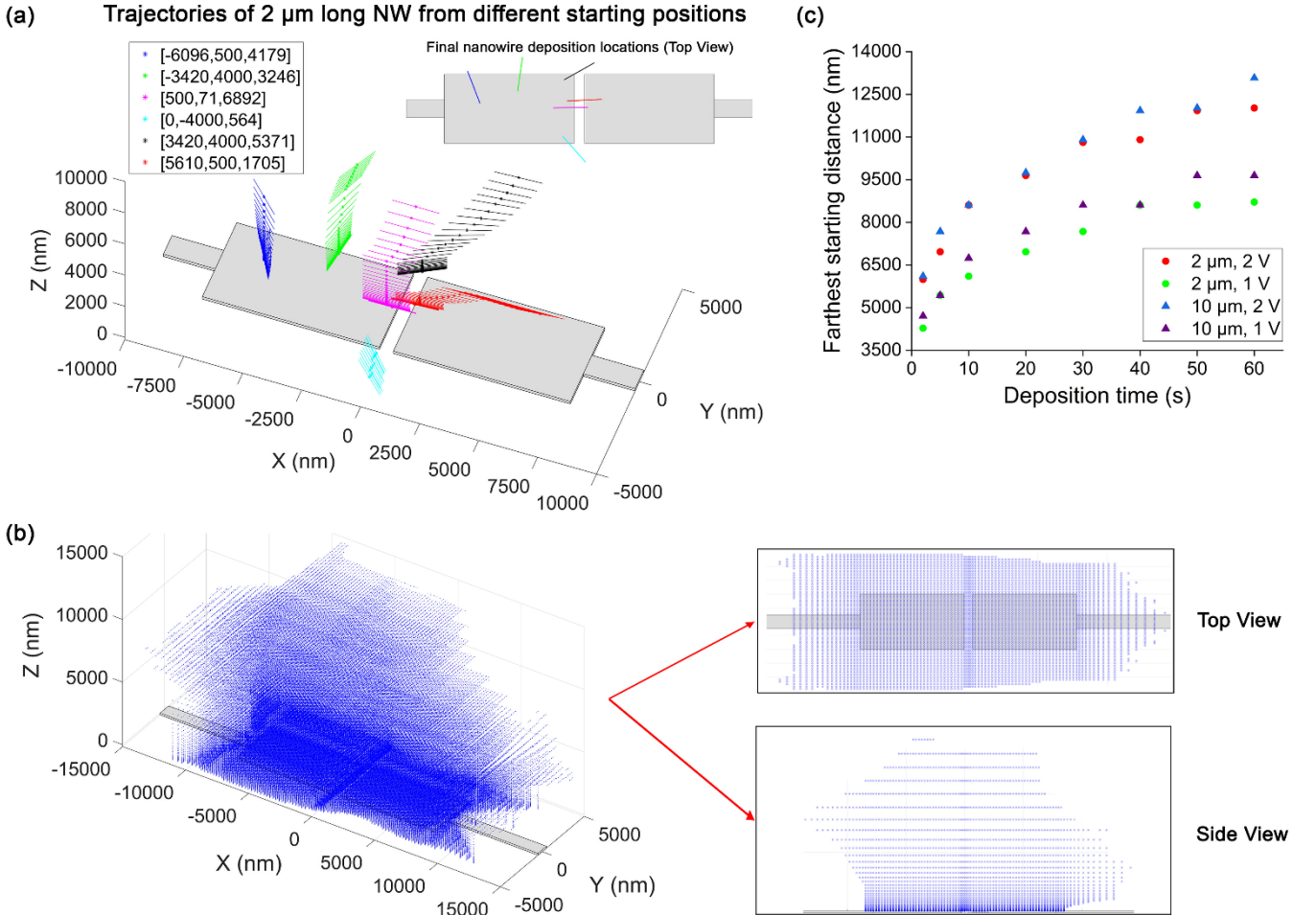

Figure 3: (a) Impact of NW starting position on its FE-DEP trajectory and eventual deposition location. The figure legend indicates the Cartesian coordinates of the NW starting positions, (b) Region of influence – ROI (insets show the top view and side view of this ROI), (c) Impact of NW length, assembly bias, and deposition time on the farthest distance from which NWs can be attracted to yield assembly at the center of the inter-electrode gap region (i.e., the (0 µm, 0 µm) position at the electrode surface plane).

bridges the gap between the two electrode locations and results in a favourable assembly outcome. It is important to note that the orientation of the deposited NW is determined by the NW initial orientation at its starting position within the suspension and by the torque it experiences along the assembly trajectory. Since the NW initial orientation is unknown, the model presented here assumes that the NW instantaneously electro-orients itself along the field lines at the starting position and then calculates the orientation at each point in its trajectory through the use of the electro-orientation torque given in Equation 7. It is important to note that this assumption is justified in the context of this work since the NW initial orientation does not alter any of the following outputs, which represent the key contributions from our model: (i) NW manipulation trajectory, and (ii) its potential starting location within the suspension for a given NW center-of-mass location at its eventual deposition / localization site on the electrodes.

In addition, Figure 3(b) shows a plot of all potential starting locations within the FE-DEP workspace from which NWs will be trapped at the electrodes at the end of a 2-minute deposition time period. This plot includes deposition at both, the inter-electrode gap (i.e., desired) and single-electrode edge (undesired) regions. It is interesting to note that even though the NWs are trapped preferentially at the biasing electrode locations, the overall volume envelope for starting positions from which they are captured remains nearly symmetric with respect to the biasing / floating electrodes (Figure 3(b)). In this report, this volume envelope for starting positions that yield NW assembly at the electrode sites is called as the electrokinetic region of influence (ROI).

The FE-DEP system involves a complex nanomanipulation process that is governed by multiple deposition parameters such as NW size, deposition time, excitation bias, and NW starting position within the workspace. All of these parameters together determine the eventual site at which the NW gets localized on the electrodes at the end of the deposition process. The impact of these parameters on the assembly process has been evaluated and summarized in Figure 3(c). In this plot, the farthest distance from which a NW can be attracted to deposit at the center of the electrode gap region is shown as a function of the deposition time. It can be seen that an increase in bias voltage and deposition time leads to an increase in the farthest distance from which a NW can be attracted and deposited in the electrode gap region. This is expected as the DEP force $\propto |E|^2$ and hence, increases with increasing voltage. However, the progressive increase in farthest starting distance diminishes with an increase in deposition time, as the force also diminishes with increasing distances, thereby reducing the velocity at farther locations. Furthermore, an increase in NW length does not significantly increase the farthest distance from which that NW can be pulled to yield assembly at the electrode sites. This is because the NW velocity $\propto \ln\left(l/r\right)$,

so an increase in NW length from 2 μm to 10 μm (i.e., by a factor of 5) only increases the velocity by 30%.

3. Results and Discussion

In order to assess the validity of the computational model, it has been compared with FE-DEP experimental results. The FE-DEP experiments involving α-MnO$_2$ NWs in ethanol were performed using the procedure described previously in the context of Figure 1 (further details on this experimental procedure can also be found elsewhere in our past reports [4, 27, 29]). In these experiments, each chip was comprised of an array of 49 electrode pairs. These electrode pairs had the same geometry and configuration as used in the computational model. Furthermore, two sets of experiments were carried out at different bias voltages of 1.5 V$_{p-p}$ (peak to peak) and 2 V$_{p-p}$, respectively. The excitation frequency and deposition time were maintained at 1 MHz and 2 minutes, respectively.

Figure 4(a) and 4(e) show the representative NW depositions across an electrode pair at excitation voltages of 1.5 V and 2 V, respectively. As can be seen, the nanowire deposition is found to occur in three different configurations: (i) localization on the biasing electrode, which represents the predominant deposition mode, (ii) bridging the biasing and floating electrode pair, which is the desired configuration and represents a successful outcome for the experiment, and (iii) localization on the floating electrode, which is also a failure mode for the process and occurs only in isolated locations. For each NW that is localized in one of the three deposition configurations described above, the computational model was used to determine the farthest NW starting position in the simulation workspace and its trajectory towards final deposition were computed (Figure 4(b-c) and 4(f-g)). It can be observed that the model is able to find potential NW trajectories that yield localization at every experimentally observed site (based on the post-assembly location of the NW center of mass). Furthermore, for the NWs summarized in Figure 4, the final orientation (i.e., post-deposition) exhibited an average difference of 2.5° for NWs that bridge the inter-electrode gap and 29.9° for NWs that are cantilevered on the electrode sites (with an overall, average orientational error of 20°). Thus, we see that this variance is less for the bridging NWs, which represent the desired assembly outcome, and is more pronounced for cantilevered NWs. In addition to the uncertainty in knowing the NW initial orientation at its starting position within the suspension (as discussed previously), the specificity of this behavior with cantilevered NWs may be attributed to local variation in electrode surface roughness or edge corrugations (that results in localized field maxima at specific pinning points on the surface) or to the sliding of NWs after the first point-of-contact on the electrode surface.
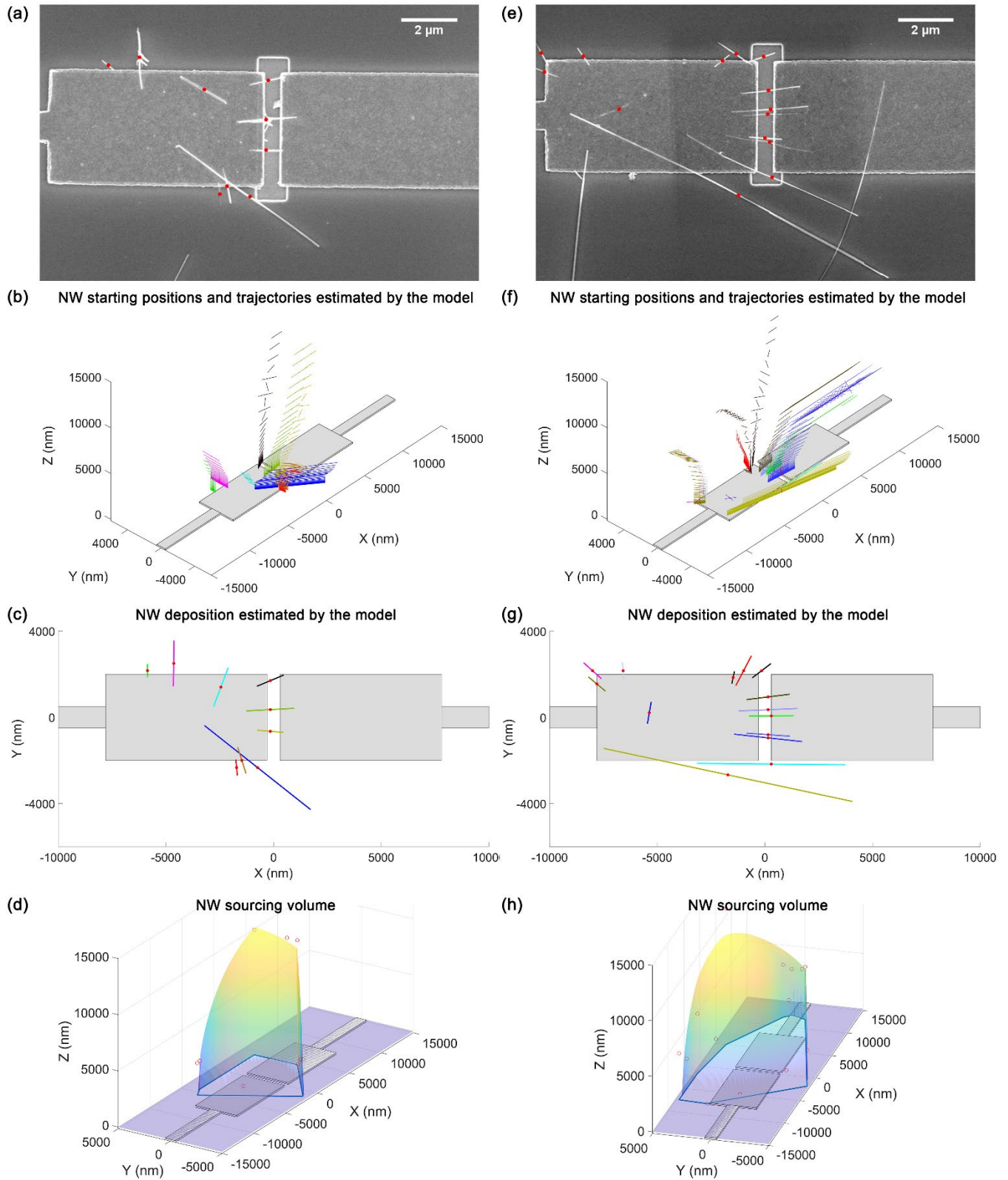
Figure 4: (a) SEM image showing the NW deposition at a representative electrode site for the 1.5 V biasing condition, (b) the computationally predicted trajectory and starting location for each NW observed to deposit in panel 'a', (c) NW deposition, as predicted by the model. Red dots on the NWs in panels 'a' and 'c' indicate their respective center-of-mass. It can be seen that for each NW localization site (as fixed by its center-of-mass), the model is able to find suitable starting positions and trajectory under the given deposition conditions, (d) sourcing volume for NWs deposited in panel 'a', (e-g) Experimental and modelling results for a representative electrode deposition site under the 2V biasing condition. The data in these four panels is analogous to those in panels 'a' through 'd'.

Another important metric that can be estimated from the computational model relates to the localized NW mass concentration at each electrode site. In order to compute this metric, the volume of space from which NWs are sourced for deposition at each electrode site is determined. This volume for a given electrode deposition site is, in-turn, estimated by finding the region of space that envelopes the farthest possible starting positions for each deposited NW at that site. This enveloping volume has been calculated using the following steps: (a) least-square fitting of a hemispherical surface (using MATLAB) to the farthest starting points for all the NWs deposited on the given electrode pair, (b) determination of a convex hull based on the X- and Y- coordinates of all the NW starting locations, and (c) evaluating the volume of space that is sandwiched between the hemispherical surface and the convex hull. The truncated hemispheres for the 1.5V and 2V deposition conditions, which were determined using the procedure above, are shown in Figure 4(d) and 4(h),

respectively. The dark blue line in the XY plane of these panels shows the convex hull construction for each of these two cases. Apart from the NW source volume, the total mass of the deposited NWs at each electrode site can be determined from their size (i.e., nominal diameter of 20nm and length, which is estimated from SEM images using an image processing algorithm in MATLAB) and crystallographic mass density (which is 4.34 g/cc for α-MnO_2 NWs). Using this procedure, the local NW sourcing volume, total mass of deposited NWs, and the NW mass concentration were determined to be 3.96×10^{-10} cc, 2.42×10^{-14} g, and 6.10×10^{-5} g/cc, respectively for the representative electrode site of Figure 4(a-d) [under the 1.5V deposition condition]. Similarly, the local NW sourcing volume, total mass of deposited NWs, and the NW mass concentration were determined to be 8.32×10^{-10} cc, 5.06×10^{-14} g, and 6.08×10^{-5} g/cc, respectively for the representative electrode site of Figure 4(e-h) [under the 2V deposition condition]. It is
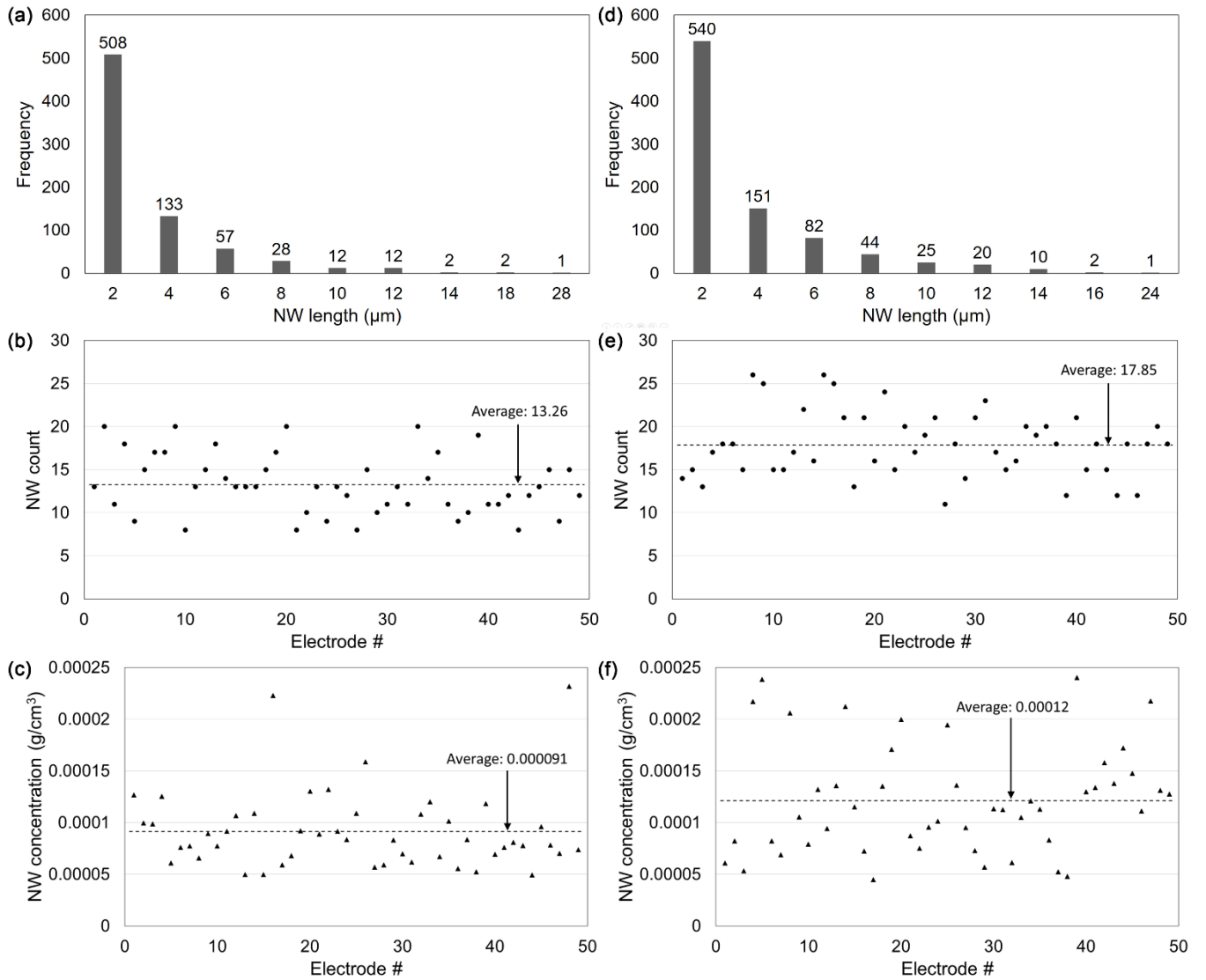

Figure 5: Summary of FE-DEP results from electrode arrays. (a) Observed distribution of lengths in the NWs, which were deposited in the electrode array, under the 1.5V biasing condition, (b) Variation in number of NWs deposited at each of the 49 electrode pairs under the 1.5V biasing condition, (c) Variation in the NW concentration at each of the 49 electrode pairs under the 1.5V biasing condition, (d-f) Summary of FE-DEP array results for the 2V biasing condition. The data in these three panels is analogous to those in panels 'a' through 'c'.

important to note that, while the overall mass concentration of NWs in our homogenized suspension is expected to remain nearly the same at every electrode site and every deposition condition, the NW mass and sourcing volume are anticipated to vary due to localized differences in the number and size of NWs that are obtained at every electrode site (these are expected due to a large variation in NW lengths within synthesized powder sample, as seen in the SEM images of Figure 4 and as will be discussed further in Figure 5 later).

The comparison between experimental results and computational predictions for 49 electrode locations has been summarized in Figure 5 for both, the 1.5V and 2V deposition conditions. Figure 5(a) summarizes the length distrbution observed among the 755 NWs, which were deposited in total across the 49 electrode pairs for the 1.5V condition. Similarly, Figure 5(d) summarizes the length distribution observed among the 875 NWs, which were deposited across the 49 electrode pairs under the 2V deposition condition. Nanowires of varying lengths have been deposited because the colloidal suspension is created from ultrasonication of a powder containing a heterogenous distribution of NW lengths, which vary in range predominantly between 1-12 μm (with occasional outliers outside this range). Figure 5(b) and 5(e) depict the total number of NWs deposited at each of the 49 electrode locations involved in the two experiments. From these panels, it is evident that an average of 13.2 NWs per electrode and 17.8 NWs per electrode have been deposited under the 1.5 V and 2 V biasing conditions, respectively. Again, this is in accordance with our model, since a higher

bias creates a larger region of influence and thereby, attracts a larger number of NWs to the electrode. Lastly, for each of the 49 electrode pairs at the two deposition condition, the volume envelope from which NWs are sourced, total mass of all deposited NWs, and the corresponding local mass concentration of NWs at that particular electrode site have been calculated (using the method described in Figure 4). The calculated values for the NW mass concentration in the colloidal suspension for each electrode site has been summarized in Figure 5(c) and (f), respectively. From this data, we compute the average NW concentration at each electrode site to be $9.13\pm1.08 \times 10^{-5}$ g/cc and $12.11\pm1.51 \times 10^{-5}$ g/cc for the 1.5V and 2V biasing conditions, respectively. It is important to note that the estimated averages for the NW mass concentration in the colloidal suspension is within ~32% of each other for the two deposition conditions. These estimations are reasonably close to each other, as would be expected from experiments that involved pipetting of NW suspensions from the same sonication vial (i.e., sample) and thereby, support the validity of our modeling approach as well as its underlying assumptions.

With the validity of our modeling approach clearly established, a strategy for realizing scalable and high-yield deposition of single NWs in the desired inter-electrode bridging configuration is outlined. As established earlier, deposition is observed on the electrode sites in three distinct configurations: biasing electrode deposition, floating electrode deposition, and inter-electrode (or, bridging) deposition. To be able to realize this objective of selective
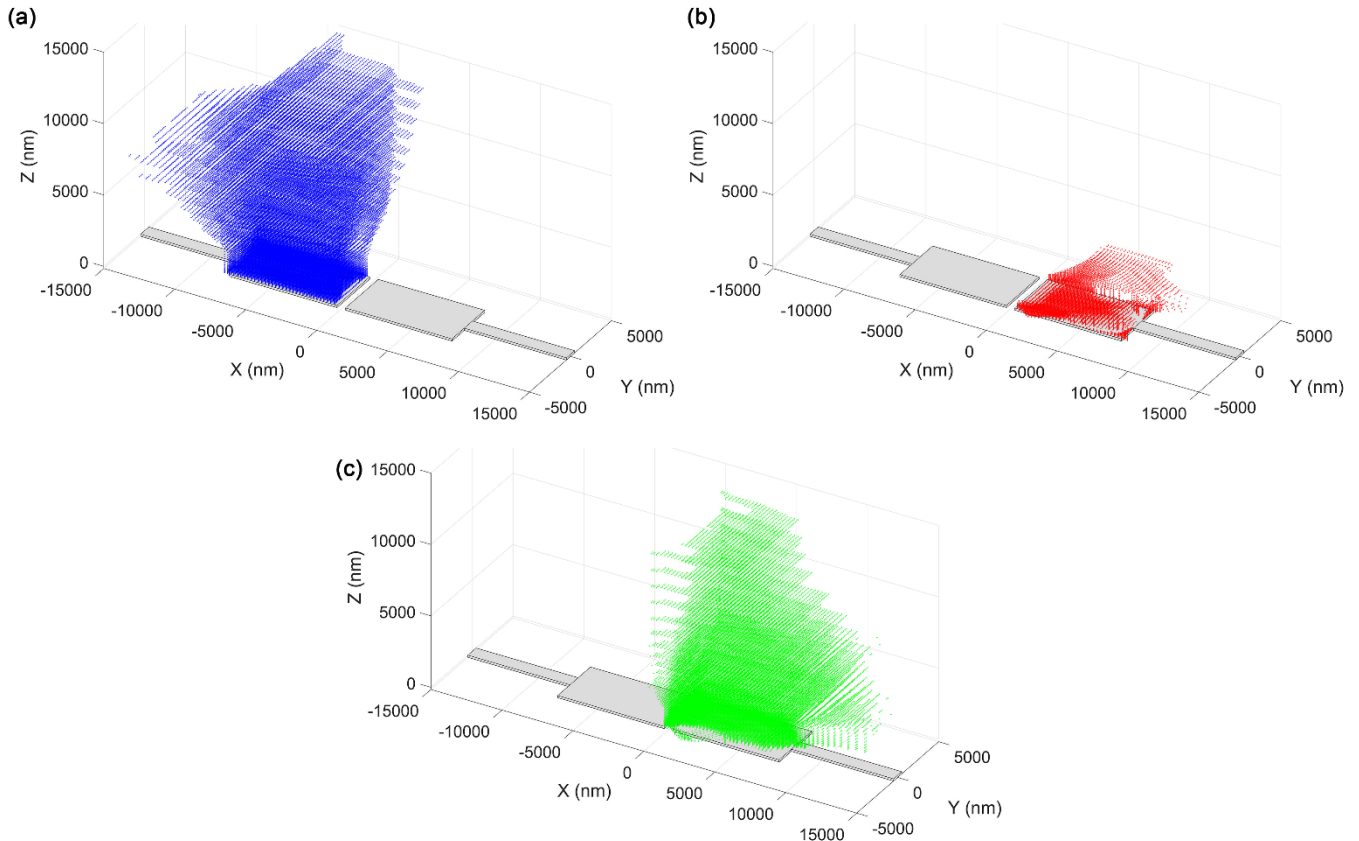

Figure 6: Potential starting locations for NW deposition such that their post-assembly center-of-mass is located (a) at the biasing electrode, (b) at the floating electrode, and (c) within the inter-electrode gap region.

deposition in the preferred inter-electrode bridging configuration, it is important to first identify the regions from which NWs are sourced for assembly at each of the three configurations and then, devise a fluidic reservoir that blocks the presence of the NW suspension from workspace regions that yield deposition at undesired sites. This is shown in Figure 6(a-c). Using our computational model, we have estimated all the locations in our simulation domain from which a NW (2 μm long and 20nm in diameter) can start and deposit in each of these three configurations, when FE-DEP is carried out at the following parameters: 2V bias at a 1 MHz frequency and over a 2 minute deposition time period. The predicted starting locations from which NWs may originate to yield deposition on the biasing electrode are shown in Figure 6(a). It can be seen that the NWs, which originate from the region directly above the floating electrode do not move and deposit over the biasing electrode. In addition, there are very few starting locations from which a NW can originate and deposit on the floating electrode under the same FE-DEP parameters (Figure 6(b)). This is because most DEP force vectors are directed away from the surface of the floating electrode, as seen earlier in Figure 2(e). As a result, only a few locations near the edge of the floating electrode are capable of yielding NW deposition at these sites. Lastly, for NW deposition in the inter-electrode gap region, the NWs originate predominantly from locations that are above the floating electrode, as seen in Figure 6(c). None of the NWs that are deposited in the inter-electrode, bridging configuration are sourced from regions directly above the biasing electrode. This asymmetric nature of the NW sourcing volume for FE-DEP nanomanipulation is leveraged to build a strategy for selective deposition in the desired inter-electrode, bridigng configuration.

We fix the desired region for single NW deposition in the inter-electrode bridging configuration as a rectangle of dimensions 600 nm × 3000 nm, which is centered with respect to the electrode pair as shown Figure 7(a). It is important to note that this window represents the region within which the NW center-of-mass needs to be located post-assembly (and not the entire length of the NW, which at 2μm is longer than the 600nm width of this window). In order to achieve the deposition of exactly one isolated NW within this rectangular window of interest, it is essential to control not only the NW sourcing region / volume, but also its deposition time and suspension concentration. Assuming a deposition time of 10 seconds, the regions within the FE-DEP workspace that represent potential NW starting locations for assembly within the rectangular window of interest is shown in Figure 7(b). The X-, Y- and Z- coordinates of the volume within which the fluid needs to be confined in order to restrict NW assembly to occur at the rectangular window of interest is defined by this region in Figure 7(c).

The NW sourcing volume can be controlled by lithographically patterning a reservoir within a polymeric resist layer that confines the NW suspension to the region defined in panel 'b'. We find the dimensions of this reservoir opening to be 5500nm × 3000nm in lateral dimensions and it needs to measure 8000nm in height (Figure 7(c)). It is important to note that the reservoir opening needs to be positioned asymmetrically and have a larger areal overlap over the floating electrode region, as shown in panel 'c'. Furthermore, in order to yield deposition of exactly one NW, the suspension in the rectangular well should hold just one NW. Assuming a uniform NW length of 2 μm and a diameter of 20nm (which is a requirement for the synthesis process), this represents a required mass concentration for NWs in the colloidal suspension of 1.68×10^{-5} g/cc.

As seen in Figure 7(b), the potential NW starting locations form a volumetric region that is not perfectly rectangular. Thus, if the NW is present in the resist reservoir within a region that is outside of this volume envelope in panel 'b', it
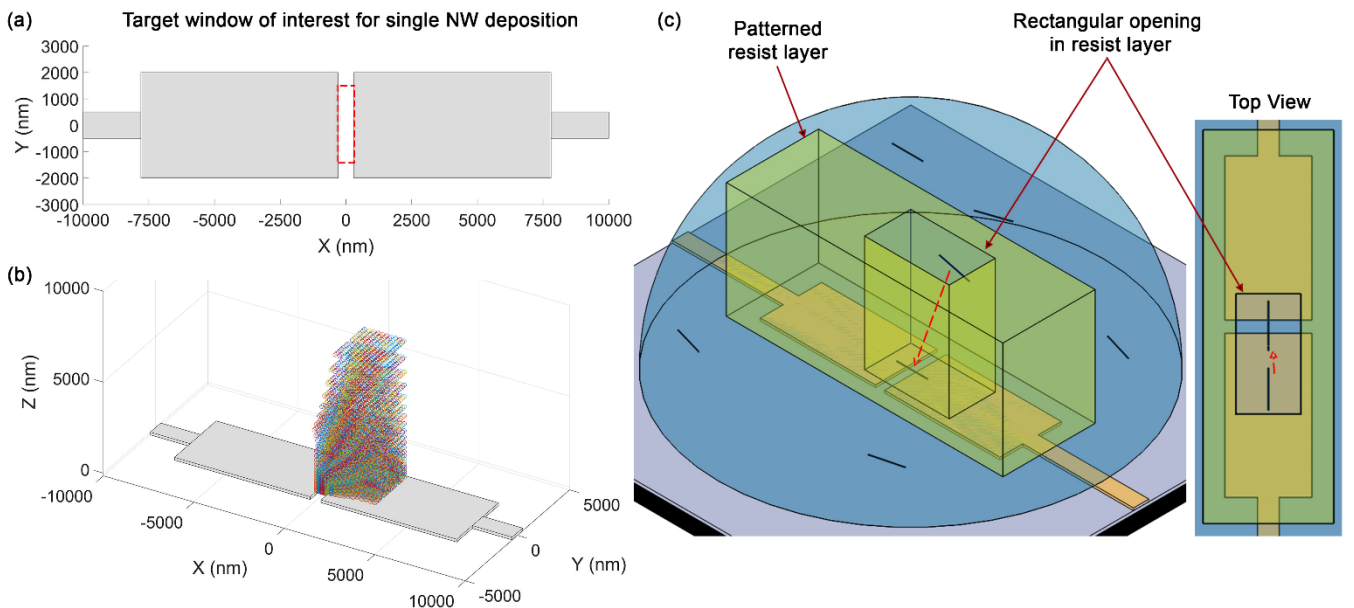

Figure 7: High-yield, single 2 μm NW deposition within a target region of interest in the inter-electrode bridging configuration. (a) Schematic illustration of target rectangular window within which single NW deposition is desired, (b) Potential NW starting positions for yielding NW assembly in the target window of panel 'a' over a 10-second deposition at 2V bias and 1MHz frequency, (c) Design of the resist reservoir.

will not yield successful assembly. Based on the ratio of these two volumes in panels 'b' and 'c', we can thus calculate the probability of successful single-NW assembly in the inter-electrode bridging configuration and within the rectangular window of interest defined by panel 'a'. This is computed as 87% and represents the estimated yield for successful single-NW deposition within a given electrode array. Furthermore, this deposition requires a homogneous suspension of $2\mu m$ long α-MnO_2 NWs in ethanol at a concentration of 1.68×10^{-5} g/cc, and the FE-DEP process involves the delivery of a 2V bias at 1MHz frequency and over a deposition time period of 10 seconds. It is important to note that this effort has presented a new approach for high-yield assembly of single NW arrays and is different from isolated past reports that have used either capillary or flow-assisted DEP techniques to realize similar high yields [13, 17].

4. Conclusion

A 3-D nanoelectrokinetic model has been presented to study the assembly of nanomaterials on to pre-patterned electrode pair arrays using FE-DEP. This comprehensive model accounts for all relevant process parameters such as electrode design, applied electric field, NW size, NW starting position in the fluidic workspace, suspension concentration, and deposition time, in order to evaluate their impact on the resultant NW trajectory and its deposition location on the electrodes. The model has been validated with direct comparisons involving the FE-DEP manipulation of α-MnO_2 NWs, which are relevant for multiple technological applications such as energy storage, catalysis, and molecular sieves. Finally, a novel strategy has been presented for high-yield assembly of single NWs arrays, which revolves around a strategy of identifying and sourcing NWs from regions which yield their FE-DEP localization at the desired target sites. This approach lends itself to designing assembly platforms for ultra-high precision assembly of any nanomaterial system, and is anticipated to advance the integration of FE-DEP nanoassembly based unit-processes with other silicon nanomachining process flows.

Acknowledgements

References

[1] H. Zhao, X. Ma, J. Bai, Z. Yang, G. Sun, Z. Zhang, X. Pan, W. Lan, J. Y. Zhou and E. Xie, *Nanoscale*, 2017, 9, 8192.

[2] X. Xia, J. Zhan, Y. Zhou, X. Wang, J. Tu and H. J. Fan, *Small*, 2017, 13, 1602742.

[3] C.-C. Lin, S.-Y. Wang, W.-L. Lin, Y.-L. Lin, C. Cheng, W.-H. Sun, Z.-L. Chen, C.-H. Chien and F.-H. Ko, *Int. J. Electrochem. Sci.*, 2015, 10, 7192.

[4] A. Subramanian, N. S. Hudak, J. Y. Huang, Y. Zhan, J. Lou and P. Sullivan, *Nanotechnology*, 2014, 25, 265402.

[5] F. Hennrich, W. Li, R. Fischer, S. Lebedkin, R. Krupke and M. M. Kappes, *ACS Nano*, 2016, 10, 1888.

[6] H. K. Park, S. W. Yoon, Y. J. Eo, W. W. Chung, G. Y. Yoo, J. H. Oh, K. N. Lee, W. Kim and Y. R. Do, *Sci. Rep.*, 2016, 6, 28312.

[7] C. Zhu, A. Chortos, Y. Wang, R. Pfattner, T. Lei, A. C. Hinckley, I. Pochorovski, X. Yan, J. W.-F. To, J. Y. Oh, J. B.-H. Tok, Z. Bao and B. Murmann, *Nature Electronics*, 2018, 1, 183.

[8] J. Jian, X. Guo, L. Lin, Q. Cai, J. Cheng and J. Li, *Sens. Actuators, B*, 2013, 178, 279.

[9] J. Suehiro, N. Nakagawa, S. Hidaka, M. Ueda, K. Imasaka, M. Higashihata, T. Okada and M. Hara, *Nanotechnol.*, 2006, 17, 2567.

[10] C. G. Nunez, A. G. Marin, P. Nanterne, J. Piqueras, P. Kung and J. L. Pau, *Nanotechnol.*, 2013, 24, 4150702.

[11] Z. Yang, M. Wang, Q. Zhao, H. Qin, J. Li, X. Li and J. Shao, *ACS Appl. Mater. Interfaces*, 2017, 9, 22837.

[12] D. Xu, A. Subramanian, L. Dong, and B. J. Nelson, IEEE Trans. *Nanotechnol.*, 2009, 8, 449.

[13] M. Collet, S. Salomon, N. Y. Klein, F. Seichepine, C. Vieu, L. Nicu and G. Larrieu, *Adv. Mater.*, 2015, 27, 1268.

[14] A. Subramanian, A. R. Alt, L. Dong, B. E. Kratochvil, C. R. Bolognesi and B. J. Nelson, *ACS Nano*, 2009, 3, 2953.

[15] Q. Cao, S.-J. Han and G. Tulevski, *Nature Communications*, 2014, 5, 5071.

[16] F. Zheng, X. Yang, Y. Wu, Z. Zhou and Z. Liu, *Carbon*, 2017, 124, 693.

[17] E. M. Freer, O. Grachev, X. Duan, S. Martin and D. P. Stumbo, *Nat. Nanotechnol.*, 2010, 5, 525.

[18] D. Wang, R. Zhu, Z. Zhou and X. Ye, *Appl. Phys. Lett.*, 2007, 90, 103110.

[19] S. Raychaudhuri, S. A. Dayeh, D. Wang and E. T. Yu, *Nano Lett.*, 2009, 9, 2260.

[20] O. Trotsenko, A. Tokarev, A. Gruzd, T. Enright and S. Minko, *Nanoscale*, 2015, 7, 7155.

[21] B. Wang, Y. Ma, N. Li, Y. Wu, F. Li and Y. Chen, *Adv. Mater.*, 2010, 22, 3067.

[22] P. J. Pauzauskie, A. Radenovic, E. Trepagnier, H. Shroff, P. Yang and J. Liphardt, *Nat. Mater.*, 2006, 5, 97.

[23] A. Jamshidi, P. J. Pauzauskie, P. J. Schuck, A. T. Ohta, P. Chiou, J. Chou, P. Yang and M. C. Wu, *Nat. Photonics*, 2008, 2, 86.

[24] O. M. Marago, P. H. Jones, P. G. Gucciardi, G. Volpe and A. C. Ferrari, *Nat. Nanotechnol.*, 2013, 8, 807.

[25] Z. Zhu, N. Wei, H. Xie, R. Zhang, Y. Bai, Q. Wang, C. Zhang and S. Wang, *Sci. Adv.*, 2016, 2, e1601572.

[26] B. R. Burg, V. Bianco, J. Schneider and D. Poulikakos, *J. Appl. Phys.*, 2010, 107, 124308.

[27] N. K. R. Palapati, E. Pomerantseva and A. Subramanian, *Nanoscale*, 2015, 7, 3109.

[28] Q. Tao, F. Lan, M. Jiang, F. Wei and G. Li, *J. Nanopart. Res.*, 2015, 17, 306.

[29] B. W. Byles, N. K. R. Palapati, A. Subramanian and E. Pomerantseva, *APL Mater.*, 2016, 4, 046108.

[30] V. Aravindan, M. V. Reddy, S. Madhavi, G. V. S. Rao and B. V. R. Chowdari, *Nanosci. Nanotechnol. Lett.*, 2014, 4, 724.

[31] Y. F. Shen, R. P. Zerger, R. N. DeGuzman, S. I. Suib, L. McCurdy, D. I. Potter and C. L. O'Young, *Science*, 1993, 260, 511.

[32] Y. Gao, Z. Wang, J. Wan, G. Zou and Y. Qian, *J. Cryst. Growth*, 2005, 279, 415.

[33] H. Ding, J. Shao, Y. Ding, W. Liu, H. Tian and X. Li, *ACS Appl. Mater. Interfaces*, 2015, 7, 12713.

[34] B. Yang, Z. Yang, Z. Zhao, Y. Hu and J. Li, *Phys. E (Amsterdam, Neth.)*, 2014, 56, 117.

[35] A. Subramanian, L. X. Dong, B. J. Nelson and A. Ferreira, *Appl. Phys. Lett.*, 2010, 96, 073116.

[36] H. Ding, W. Liu, J. Shao, Y. Ding, L. Zhang and J. Niu, *Langmuir*, 2013, 29, 12093.

[37] T. B. Jones, "Electromechanics of Particles", Cambridge Univ. Press, Cambridge, UK, 1995.

[38] A. Subramanian, T.-Y. Choi, L. X. Dong, J. Tharian, U. Sennhauser, D. Poulikakos and B. J. Nelson, *Appl. Phys. A: Mater. Sci. Process.*, 2007, 89, 133.

[39] S. C. Harding, M. Dampier and A. J. Rowe, *IRCS Med. Sci.*, 1979, 7, 1813.

[40] E. W. Small and I. Isenberg, *Biopolymers*, 1977, 16, 1907.